

# A “slice-and-view” (FIB–SEM) study of clay gouge from the SAFOD creeping section of the San Andreas Fault at ~2.7 km depth



Laurence N. Warr<sup>a,\*</sup>, Jasmaria Wojatschke<sup>a</sup>, Brett M. Carpenter<sup>b</sup>, Chris Marone<sup>c</sup>, Anja M. Schleicher<sup>d</sup>, Ben A. van der Pluijm<sup>d</sup>

<sup>a</sup> Institut für Geographie und Geologie, Ernst-Moritz-Arndt Universität Greifswald, F.L. Jahn-Str. 17a, 17487 Greifswald, Germany

<sup>b</sup> INGV, Rome 1, Section, Via di Vigna Murata 605, Rome 00143, Italy

<sup>c</sup> Department of Geosciences, Center for Geomechanics, Geofluids, and Geohazards, The Pennsylvania State University, University Park, PA 16802, USA

<sup>d</sup> Department of Earth and Environmental Sciences, University of Michigan, 1100 University Ave, Ann Arbor, MI 48109, USA

## ARTICLE INFO

### Article history:

Received 10 July 2014

Received in revised form

6 October 2014

Accepted 14 October 2014

Available online 28 October 2014

### Keywords:

Creep

Clay fabric

Mg-smectite

San Andreas fault

SAFOD

FIB–SEM and TEM

## ABSTRACT

The San Andreas Fault is one of the most studied earthquake-generating structures on Earth, but the reason that some sections are anomalously weak, and creep without apparent seismicity, remains poorly understood. Here, we present results from nanoscale (FIB–SEM) 3D microstructural observations of weak (friction coefficient of 0.095) SAFOD clay fault gouge containing serpentinite clasts, recovered from the active Central Deforming Zone at ~2.7 km vertical depth. Our nanoscale observations confirm that frictional slip and extreme weakness occur via deformation of smectite clay that forms a shear fabric within the fault zone. We infer that creep initiates by fracture-controlled, substrate growth of oriented Mg-smectite on R, P and Y shears, followed by clay smearing and ductile flow of an evolving and expanding clay matrix. At the crystal-scale, pervasive sliding occurs along hydrated smectite interlayers and surfaces occupied by exchangeable Mg- and Ca-ions, with slip typically spaced at 3–5 lattice layers apart. We conclude that the strength and seismic behaviour of major tectonic faults at shallow crustal levels evolves as clay fabric develops with accumulated fault slip.

© 2014 Elsevier Ltd. All rights reserved.

## 1. Introduction

Active faults are inherently weak structures of the Earth's crust that cause diverse earthquake activity (Scholz, 2002; Holdsworth, 2004; Marone and Richardson, 2010). A key location to study earthquake faulting is the San Andreas Fault Observatory at Depth (SAFOD) drill site in central California, which is positioned in a transition zone between seismically active and creeping portions of the fault (Fig. 1a; Hickman et al., 2007; Zoback et al., 2011). This zone is characterized by ~25 mm/yr of creep motion, repeating micro-earthquakes (<M3) clustered along the fault at depth, and periodic rupture during M6 earthquakes (Zoback et al., 2011; Titus et al., 2006; Nadeau et al., 2004). Multiple cores recovered from the actively deforming fault zone (Fig. 1b) have provided a unique chance to study fresh fault gouge and to establish the processes responsible for the apparent fault weakness at the depth of the borehole and its creep behaviour (Zoback et al., 1987, 2011).

The hypothesis that talc causes creep at the depth of the borehole (Moore and Rymer, 2007; Wibberley, 2007) has not gained support due to the rare occurrence of this mineral in SAFOD fault gouge. Instead, agreement has emerged that creep occurs at locations characterized by the concentration of hydrous clay minerals, namely smectites, vermiculites, mixed-layered illite–smectite and chlorite–smectite phases that form by low temperature alteration of mudrock lithologies and enclosed serpentinite clasts (Schleicher et al., 2006, 2010; Solum et al., 2006; Bradbury et al., 2011; Holdsworth et al., 2011; Carpenter et al., 2011, 2012; Janssen et al., 2014). Particular emphasis has been placed on the abundance of frictionally weak trioctahedral Mg-rich smectite (saponite) caused by dissolution and precipitation alteration of tectonically emplaced serpentinite rocks and sedimentary shales along the two creeping strands of the fault as the primary cause of creep (Carpenter et al., 2011, 2012; Moore and Rymer, 2012; Moore and Lockner, 2013). More specifically the reaction is considered to have a metasomatic character, whereby significant changes in the bulk chemistry of the rock have occurred on an undefined macroscopic scale (Moore and Lockner, 2013). Others have highlighted

\* Corresponding author.

E-mail address: [warr@uni-greifswald.de](mailto:warr@uni-greifswald.de) (L.N. Warr).

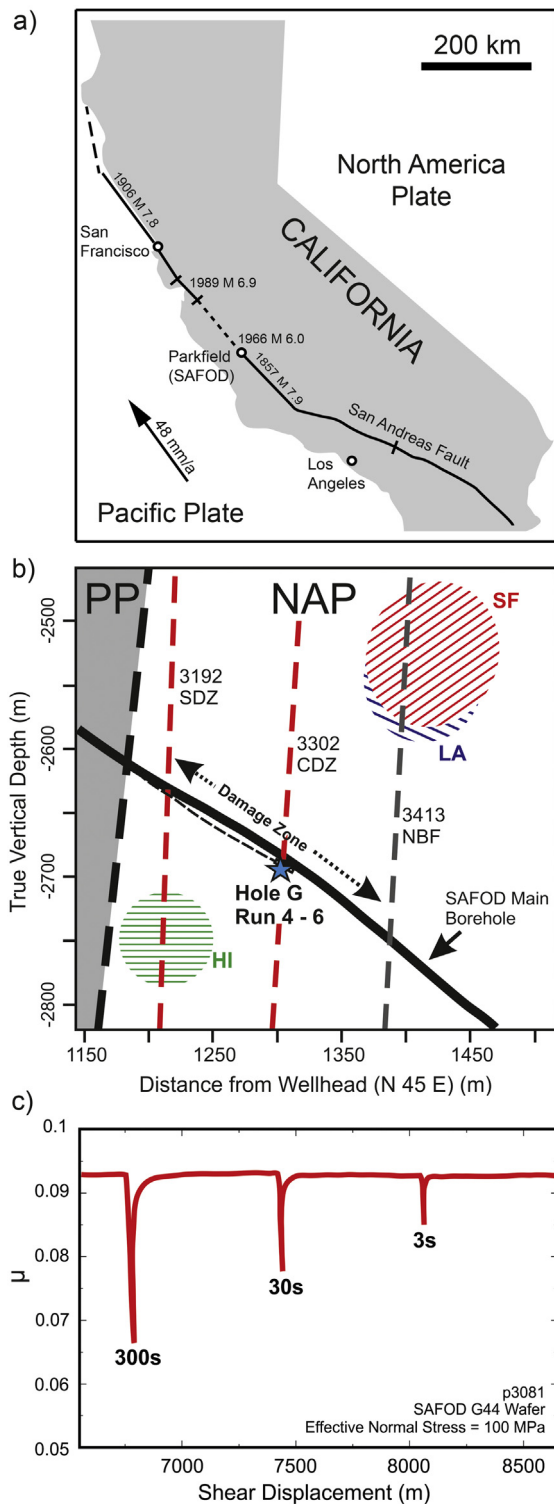


**Fig. 1.** a) Location map of California showing the position of the SAFOD project at Parkfield, along the San Andreas Fault. The drill site is at the intersection zone between a seismically active strand to the SE and a creeping section (dashed line) to the NW. b) Detailed depth profile showing the position of the SAFOD main hole (Phase II) intersecting the two actively creeping fault strands at borehole depths of ~3192 m and ~3302 m and the position of the sample studied here (star). SDZ = Southwest Deforming Zone, CDZ = Central Deforming Zone, NBF = Northern Bounding Fault, PP = Pacific Plate, NAP = North American Plate, micro-earthquake cluster: SF = San Francisco, LA = Los Angeles, HI = Hawaii (modified after Zoback et al., 2011). c) Frictional behaviour of sample G44 as a brine-saturated intact wafer, sheared at an effective normal stress of 100 MPa, and with a slide–hold–slide sequence, in reverse order, of 300, 30 and 3 s.  $\mu$  = friction coefficient.

the importance of the site-specific arrangement of various smectitic phases along interconnected, pervasively developed, and foliated networks for attaining notably low material strength (Schleicher et al., 2010; Holdsworth et al., 2011; Janssen et al., 2012). Pressure-solution creep has also been proposed to explain fault weakness at the depth of the borehole (Gratier et al., 2011). Here, clay minerals are viewed as passively concentrated due to their low solubility but are not considered to cause creep. In addition to stress-driven mass transfer, granular flow along phyllosilicate-rich Riedel surfaces in the creep gouge has also been suggested as important (Hadizadeh et al., 2012).

That foliated clay gouge can be significantly weaker than equivalent powder samples has been demonstrated in rock deformation experiments (Collettini et al., 2009; Haines et al., 2013; Ikari et al., 2011a) indicating that weak faults can occur at low concentrations of clay minerals, as long as they form an interconnected fabric. Based on electron microscopic observations of various mudrock-based gouges from the creeping zone of the SAFOD borehole, it was also proposed that smectite-coated foliated slip surfaces occur at the nanometre-scale, and were termed “clay nanocoatings” (Schleicher et al., 2010). However, one commonly stated problem of the clay (phyllosilicate) fabric hypothesis of creep is that a number of laboratory experiments found that the strength of fault rock is determined primarily by the clasts between the shear fabric surfaces (Bos and Spiers, 2001; Niemeijer and Spiers, 2006; Niemeijer et al., 2010; Ikari et al., 2011b). Therefore, a mechanism is required to maintain slip on selected shears without fracturing intervening clasts that would produce strain-hardening behaviour.

A principal restriction for understanding the mechanisms associated with slip surfaces in creeping fault gouge has been the analytical difficulty of resolving detailed structural and chemical information from such specific locations. A number of general optical- and scanning electron-microscopy studies have described the 2D nature of both microstructures and microchemistry from the hand-specimen scale down to the micrometre-scale (e.g. Bradbury et al., 2011; Holdsworth et al., 2011). Also, a number of higher resolution transmission electron microscope (TEM) studies for select samples close to, but not precisely within the active deforming zones, have extended observations down to lattice scale (Schleicher et al., 2006, 2010; Janssen et al., 2010, 2012, 2014).

In this contribution, we present results from a “slice-and-view,” focused ion beam–scanning electron microscopy (FIB–SEM) of the San Andreas Fault gouge. To the best of our knowledge, this contribution is the first such study of an extremely weak clay gouge from the actively creeping section of a major tectonic fault. This technique combines the imaging capabilities of modern field-emission SEM (resolution < 2 nm) with the polishing and milling power of FIB to reconstruct 3D microstructural and microchemical features over the range of nanometres to tens of micrometres. Using these tools, together with conventional TEM, we focus on the critical arrangement of clay-coated slip surfaces and clay fabrics to provide new insights about clay creep mechanisms and fabric evolution from the crystal lattice-scale to the scale of clay shear fabrics.

## 2. Materials and methods

We used fault gouge collected from SAFOD Hole G, run 4, section 4, core recovered from the main, actively creeping strand of the San Andreas Fault, termed the Central Deforming Zone (Hickman et al., 2007; Zoback et al., 2011). This sample, which we refer to as G44, comes from 3298 m measured borehole depth and corresponds to a true vertical depth of ~2.7 km (Fig. 1b). The precise location of the sampled core material can be viewed at <http://coreviewer>.

[earthscope.org/samples/safod\\_core\\_samples/](http://earthscope.org/samples/safod_core_samples/) in Hole G, Run 4, Section 4, between 44 and 51 cm. This part of the core was studied in detail by Sill (2010) and Carpenter et al. (2012) and is composed of sheared serpentinite clasts set in a matrix of clay that is plastic when wet. The small, cm-sized, lens-shaped serpentinite fragments are dark grey–green in colour, with outer shiny, polished surfaces coated with soft clay minerals, similar to those described in previous studies of the SAFOD fault gouge (Schleicher et al., 2010; Bradbury et al., 2011; Holdsworth et al., 2011; Carpenter et al., 2011, 2012; Moore and Rymer, 2012). This core site was selected because it represents some the weakest gouge that shows anomalously low rates of frictional healing, consistent with aseismic creep (Carpenter et al., 2009, 2011, 2012). To confirm its low strength, the G44 material was experimentally deformed in the laboratory using a true-triaxial pressure vessel within a biaxial-load frame. Intact samples were deformed in a single direct-shear configuration under conditions of constant effective normal stress, confining pressure, and pore pressure. See Carpenter et al. (2012) for detailed descriptions and schematics of the experimental apparatus and protocols.

For our study, we used small fragments (5–10 mm in size) of the original core material. For mineral identification, X-ray diffraction (XRD) analysis of selected parts of the clay matrix and examples of individual clasts were made both on random whole rocks powders and oriented slide preparations that enhanced the 00 $l$  reflections of clay minerals. Measurements were made using a Bruker D8 Advance equipped with a Lynxeye detector and a Co-X-ray tube at 40 kV and 30 mA. Analyses were supported by examination of air dried-, glycerol-, ethylene glycol and water-saturated treatments for characterizing the smectite.

Based on the XRD results, various clasts of serpentinite were chosen, most with characteristic polished clay-coated slip surfaces that bear fault striations. Soft mud matrix specimens were also selected from undisturbed material, which was broken open using a razor blade to create a fresh fracture surface. These fragments were mounted so as to image the undisturbed clay fabric and to avoid the deformation caused by the razor blade. Due to the soft nature of the gouge, microscopic study was made directly on the solid fragments and not on thin sections where the soft clay minerals are more difficult to preserve in their intact state (e.g. Holdsworth et al., 2011; Janssen et al., 2012). Specimens were mounted on carbon SEM holders in positions so that the selected areas could be accessed for study. The pieces were most commonly positioned for ion-milling into a plane lying perpendicular to the observed direction of shear as marked by fault lineations located on displacement surfaces (Fig. 3a,b). Several “slice-and-view” operations were conducted by milling down into the clasts, the characteristic polished fault surfaces of the clasts, and the slip surfaces that define the anastomosing scaly fabric of the clay matrix.

Microscope analyses were made using a Zeiss Auriga focused ion beam–scanning electron microscope (FIB–SEM) field emission instrument (resolution < 1.5 nm) equipped with a gallium ion beam for milling and an in-lens energy selective backscatter detector (BSE) for imaging of slice surfaces (Warr and Grathoff, 2011). To improve the imaging quality during “slice-and-view” study, specimens were vacuum-coated with a thin layer of palladium. Several different sample locations on each specimen were selected for study. For ion milling the working distance was set at 5 mm, the milling depth at 12  $\mu$ m and the milling current at 30 kV, 500 pA. The number of slices varied between 60 and 120, and the voxel size was set at 16  $\times$  16  $\times$  10 nm. Imaging was undertaken using an electron beam with an accelerating voltage of 5 kV and a 60  $\mu$ m aperture size and the in-lens energy and angle selective BSE detector. Energy Dispersive X-ray spectrometry (EDX) analyses were made on each ion-polished slice without changing the microscope settings using

the 3D automated mapping option of the INCA Energy 350 software of Oxford Instruments, and an extra-large 80 mm<sup>2</sup> X-Max SDD detector for improved detection of X-rays at low accelerating voltages. Due to the low voltage setting,  $L\alpha$  lines and not  $K\alpha$  lines were used for the elemental mapping of Fe. Calibration of elemental concentrations was made using internal machine standards provided by Oxford Instruments. Elemental oxide concentrations were normalized to 100%. The accuracy of elemental determinations was also tested on available polished mineral standards, and found to be <2% error (1 $\sigma$ ) for concentrations higher than 1%. 3D image analysis was made using the software AVIZO Fire version 8.0 from the Visualization Sciences Group (<http://www.vsg3d.com/avizo/fire>). The slice sequences were initially corrected for beam shift errors prior to quantitative analysis and presentation.

Lamellae for TEM study were prepared by thinning down to ~50 nm sample thickness following documented methods (Wirth, 2009; Mayer et al., 2007). The sample was recovered using a Kleindiek nanomanipulator and then transferred to a JEOL JEM 1200 TEM, with an accelerating voltage of 120 kV and a point-to-point resolution of 0.36 nm. Samples were imaged at magnifications up to 100 000 $\times$  and recorded using a GATAN Digital Micrograph Orius SC200 CCD camera with a pixel resolution of 2.0k  $\times$  2.0k. Measurements of lattice fringes were made with the measuring ruler option of the GATAN software, which had been calibrated for the selected magnifications. Due to the rapid beam damage of the clay-rich fault gouge and the formation of amorphous material, special attention was given to obtaining images as fast as possible, without prolonged exposure to the electron beam. However, naturally amorphous phases could not be separated from ion or electron-induced amorphous material (Egerton et al., 2004). Selected area electron-diffraction (SAED) patterns were performed on locations of interest, but due to the rapid beam damage the patterns disappeared within a few seconds, and therefore could not be recorded.

Quantitative study of mineral abundance and matrix porosity was made using ImageJ software <http://imagej.nih.gov/ij/>. The grey scale of BSE electron images was selected in the threshold model and then the objects measured by the area analysis function. The areas of the various grey scale objects were normalized and then expressed in % abundance. Multiple analyses were performed using the numerous slices to obtain better counting statistics. Objects with characteristic grey scale ranges could be assigned to a particular mineral phase by using EDX results. The aspect ratio of clasts in the clay matrix was determined by using a measurement tool and dividing the long by the short axes.

### 3. Results

#### 3.1. X-ray diffraction

X-ray diffraction analysis of whole-rock powders of selected clasts and soft clay matrix showed mineral assemblages composed of smectite, serpentine, chlorite, quartz, calcite and feldspar (Fig. 2). Analysis of serpentinite clasts identified fragments composed of serpentine, smectite and calcite. Others contain mostly quartz or calcite with minor amounts of smectite. The clay matrix is composed largely of smectite, quartz, with minor chlorite, calcite and feldspar (mostly albite). Analyses of oriented preparations of the clay matrix show the smectite lacks mixed-layered phases and contains mostly divalent cations with 2-water layer hydration states dominating (~0.146 nm 001 reflections) when air-dried under laboratory conditions (Moore and Reynolds, 1997). The complexation behaviour of the natural smectite in glycerol and ethylene glycol is similar to that of trioctahedral Mg-saturated

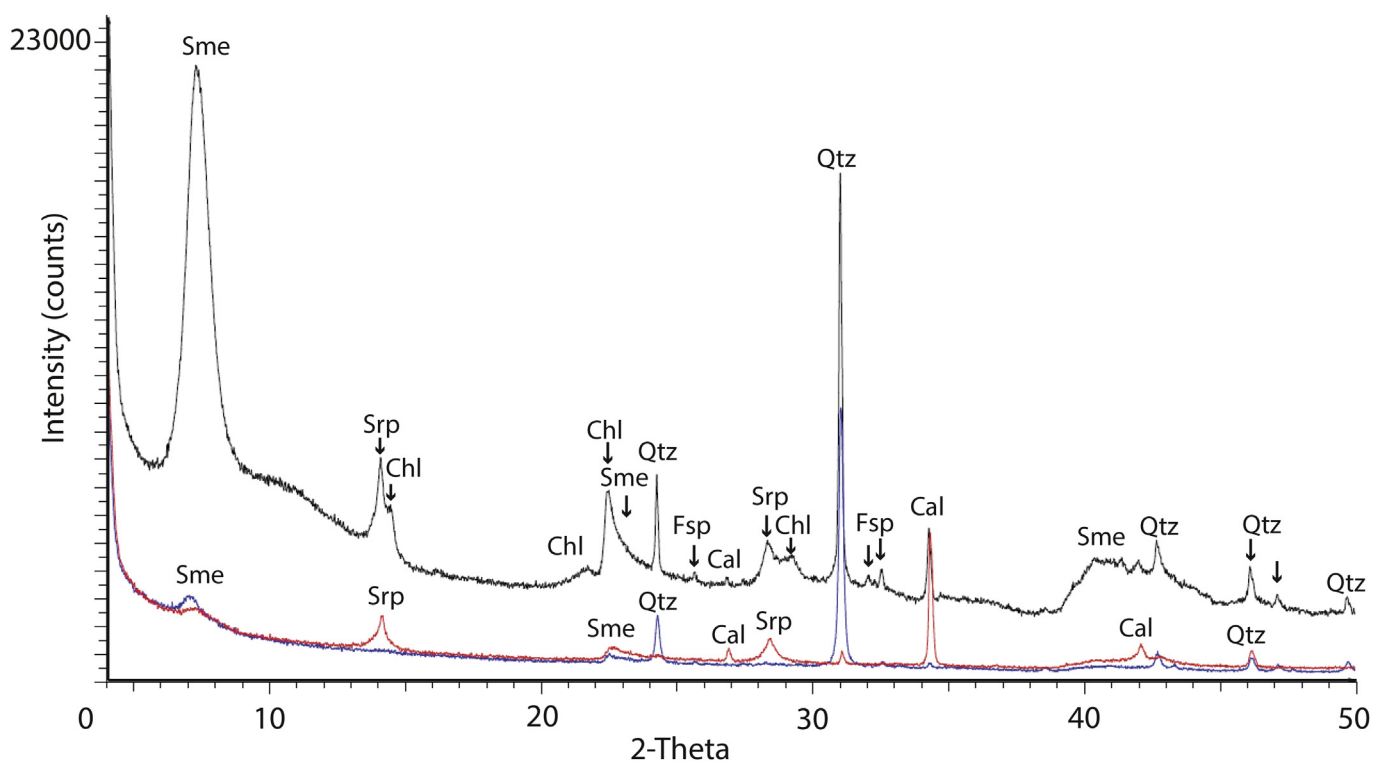


**Fig. 2.** X-ray diffraction patterns of the matrix and clast material of the G44 sample (randomly powdered preparation). Matrix = black line, clast 1 = red lines, clast 2 = blue line. Sme = smectite, Srp = serpentine, Chl = chlorite, Qtz = quartz, Cal = calcite, Fsp = feldspar. (For interpretation of the references to colour in this figure legend, the reader is referred to the web version of this article.)

saponite, using the criteria described by Suquet et al. (1975), with 001 reflections at 0.181 nm and 0.168 nm, respectively (Table 1).

### 3.2. Rock mechanical test

That this fault rock sample has the physical properties expected for creeping gouge was confirmed by laboratory experiments where the samples were deformed under brine saturated conditions and effective normal stresses of 10–100 MPa using a true triaxial pressure vessel (Carpenter et al., 2012). The intact material represents some of the weakest gouge yet recovered from SAFOD core, with a friction coefficient ( $\mu$ ) of 0.095, and friction does not increase during quasi-stationary contact but remains constant (Fig. 1c), consistent with previous data for samples recovered from this zone (Carpenter et al., 2011, 2012). As pressure-solution creep is not expected to be significant in such short-term laboratory experiments because of the relatively slow rate of mineral dissolution, it is evident that this mechanism is not the likely cause of creep in this clay gouge.

### 3.3. FIB–SEM observations

Small, ~10 mm fragments selected from the core sample were carefully prepared for “slice-and-view” study (e.g. Fig. 3a). Following initial SEM investigation, three types of material were identified and analysed in detail: i) The serpentinite clasts; ii) the clay-coatings of the serpentinite clasts with slickenfibres along the direction of movement (Fig. 3b); and iii) the soft clay matrix.

Quantitative analysis of the BSE imaged slices of intact serpentinite (Fig. 4a) shows serpentine (~78%) with smectite (~22%). EDX analysis of the serpentine yields an average composition of  $(\text{Fe}_{0.16}\text{Mg}_{2.7}\text{Al}_{0.14}\text{Na}_{0.05}\text{Ca}_{0.06})[\text{Si}_{2.03}\text{O}_5(\text{OH})_4]$ , number of analyses = 6,

indicating minor contamination by smectite (Fig. 4b). Due to the pervasive distribution of the smectite alteration, it was not possible to accurately determine its composition. 3D block diagram reconstructions of BSE images and Fe–Mg elemental maps show neither serpentine nor smectite exhibit any preferred orientation, and therefore the clast material appears largely unstrained (Fig. 5). The Mg-depleted saponite alteration appears as an alteration rim around a remnant of a serpentine grain and is also scattered in small concentrations throughout the grain itself.

Ion-milling of the clay coatings perpendicular to the slip direction and 3D reconstructions reveal a principal slip-surface and a tight network of other smectite-coated shear fractures within serpentine (Figs. 4c and 6a; movie 1, part a), equivalent to previously documented clay nanocoatings (Schleicher et al., 2010). In addition to the <200 nm thick smectite coating of the upper surface, similar alteration occurs aligned along parallel and dipping fractures, which are most abundant in the first 4  $\mu\text{m}$  beneath the principal slip surface. The thickness of the clay coatings is typically 100–1000 nm, although finer veinlets occur below the resolution of

**Table 1**  
d-values (nm) of the 001 basal reflections of smectite based on various preparation treatments. XRD patterns were calibrated using the quartz 0.4257 nm reflection.

Treatment	Natural smectite	Mg-saturated smectite	Mg-saturated saponite <sup>a</sup>
No solvation (air dried)	0.147	0.145	–
Glycerol	0.181	0.178	0.181 (0.143)
Ethylene glycol	0.168	0.168	0.167

<sup>a</sup> Results from Suquet et al. (1975). Bracketed values are characteristic subsidiary reflections.

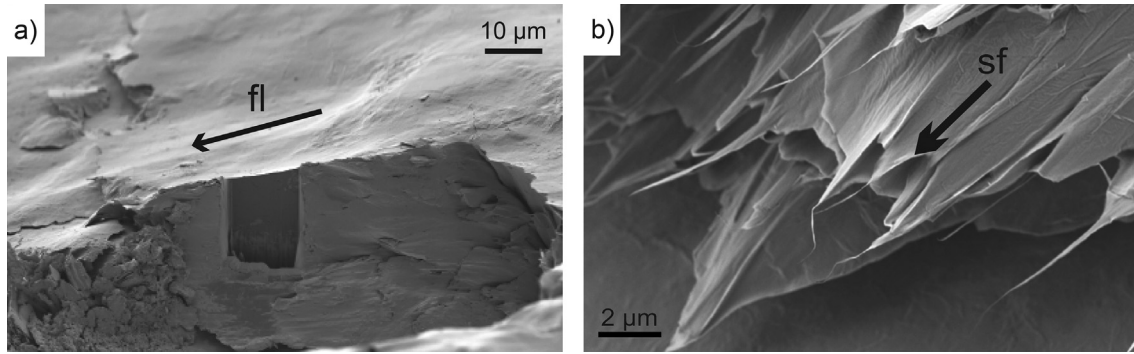


**Fig. 3.** a) Example of a polished fault surface (a principal plane of displacement) that was selected for “slice-and-view” study. The location of the cut section is shown, and was positioned perpendicular to the slip direction as marked by fault lineations (fl). The upper surface of the milled section therefore corresponds to the fault plane. b) Nature of smectite particles coating the smooth slip surfaces on serpentinite clasts imaged using secondary electrons. Note the strong alignment of partly fibrous and platy smectite particles. sf = slickenfibres.

the BSE imaging. The geometry of fracture networks shows similarities with microscopic observations of SAFOD gouge from the Southwest Deforming Zone (Hadizadeh et al., 2012) (see Fig. 1b for location), with the development of Riedel (R) and pressure (P) shears forming at low angles (10–45°) to microscopic-scale principle displacement surfaces (Fig. 6a). That some angles are >30°

may reflect some distortion of the specimen due to shrinkage effects of the smectite when placed in the microscope vacuum, as suggested by the open cracks in the sample. We note that Y shears lying parallel with the upper slip surface are also evident.

Supplementary data related to this article can be found online at <http://dx.doi.org/10.1016/j.jsg.2014.10.006>.

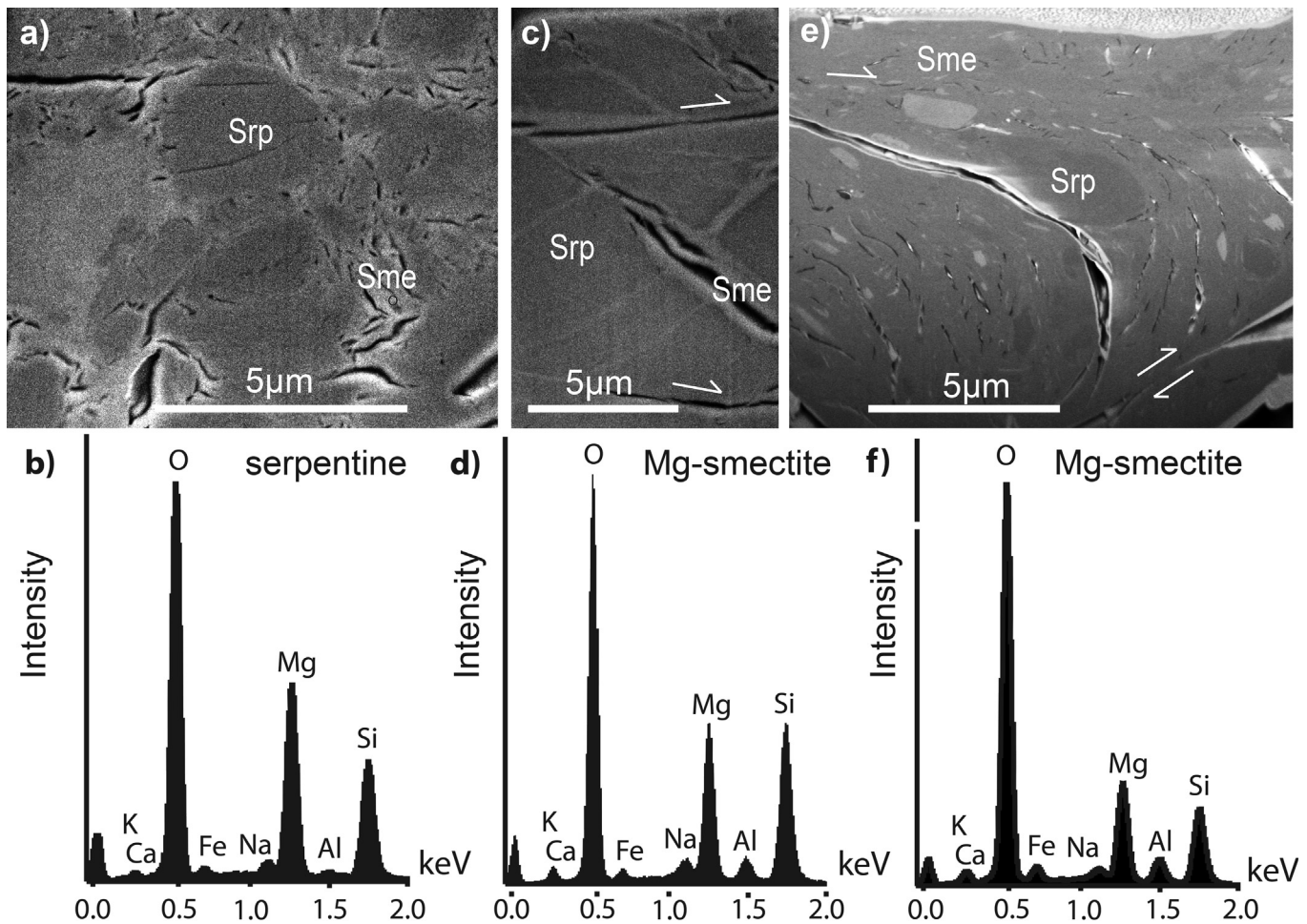


**Fig. 4.** a) BSE image of ion-polishing slice into a serpentinite clast. b) EDX spectrum of a serpentinite (serpentine) grain. c) BSE image of ion-polishing slice into the striated, clay-coated surface of a serpentinite clast showing Mg-smectite-filled shear fractures. d) EDX spectrum of Mg-smectite alteration coating the serpentinite. e) BSE image of the clay-rich matrix of the creep gouge showing folds of the clay fabric and the location of a shear plane (bottom right of image). f) EDX spectrum of the Mg-smectite in the clay matrix. Srp = Serpentine, Sme = smectite.

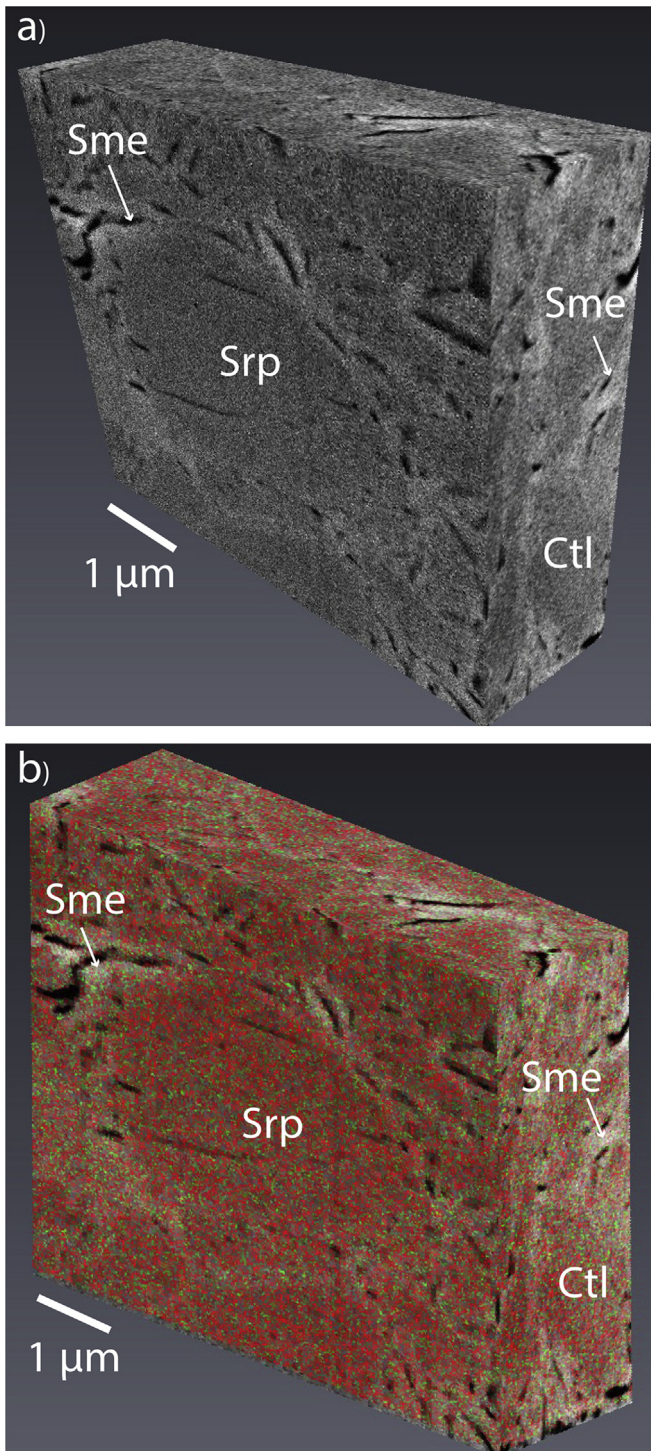


**Fig. 5.** 3D reconstructions of FIB slices of a serpentinite clast. a) BSE imaging of the darker grey serpentinite and lighter grey Mg-smectite. b) Combined Fe and Mg elemental mapping of the same volume in a). Green = Fe and red = Mg. Note the lower concentration of Mg around the margins of the central serpentinite grain. Srp = serpentinite, Sme = smectite. (For interpretation of the references to colour in this figure legend, the reader is referred to the web version of this article.)

The 3D geometry of smectite layers is also defined by depleted Fe + Mg and greater concentrations of Si and Al (Fig. 6b–d: movie 1, part b). EDX analyses (Fig. 4d) give a trioctahedral smectite (saponite) composition, with the following average structural formula  $K_{0.02} Na_{0.08} Mg_{0.11} Ca_{0.11} (Mg_{2.70} Fe_{0.28} Ni_{0.02})[(Si_{3.57} Al_{0.32} Fe_{0.11})O_{10}$

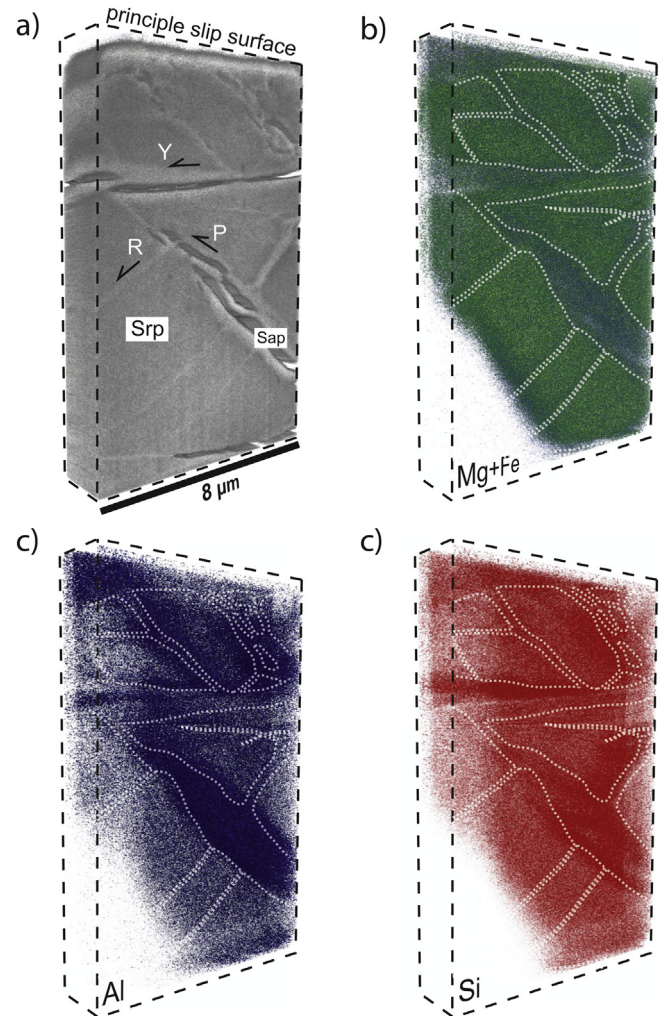


**Fig. 6.** 3D reconstructions of FIB slices of a serpentinite–smectite band lying beneath a striated fault surface. a) BSE image, b) EDX mapping of Mg (green) + Fe (blue), c) EDX mapping of Al, d) EDX mapping of Si. In all EDX plots, the darker more intense colouration is of areas of greater elemental concentrations. P = pressure (thrust) shear, R = Riedel shear, Y = shear parallel to principal slip surface. The dotted white lines mark phase boundaries. The observed open nature of the fractures is most likely an artefact of some dehydration shrinking of the smectite in the vacuum of the microscope. Srp = serpentinite, Sme = Smectite. (For interpretation of the references to colour in this figure legend, the reader is referred to the web version of this article.)

$[(OH)_2]$ , number of analyses = 4 and assuming trivalent Fe. As Ca cannot occupy either octahedral or tetrahedral sites in the clay mineral structure, this element together with Mg, are the main cations occupying the interlayer, in agreement with previously determined Mg-rich smectite compositions (Schleicher et al., 2006). However, we cannot rule out the possibility that minor contamination of the smectite analyses by serpentinite has occurred, and thus the precise amount of Mg in the interlayer remains uncertain. EDX compositions of the serpentinite show minor amounts of  $Al_2O_3$  (~1%) and CaO (<0.2%) confirming that smectite alteration also occurs within the serpentinite at a sub-micrometre level. Quantitative analysis of the BSE images and the distribution of elements across the 3D volume show smectite to account for ~30% of the ~10 µm deep slice. Ignoring the fracture porosity caused by shrinkage due to water loss in the SEM, the maximum matrix porosity is extremely low (<1%; movie 1, part c) in accordance with published porosity and permeability measurements (Janssen et al., 2010; Morrow et al., 2013). A key result of our microscopic analyses,

with important implications for the weak mechanical behaviour of the fault zone is that all resolvable fracture surfaces are coated by smectite.

“Slice-and-view” analysis of the soft clay matrix shows abundant >80% Mg-smectite with <20% clasts of serpentinite, quartz and Fe-chlorite (Fig. 4e). Local areas of the matrix also contain fragments of pyrite and calcite. The clay matrix has a well-developed fabric, which we relate to ductile deformation, with small lens-shaped clasts oriented parallel to the fabric. The aspect ratio of serpentinite clasts ranges between 1.27 and 6.2, and has an average of 2.7 (number of analyses = 108). Many clasts have notably smooth and rounded surfaces but lack evidence of internal deformation. A scaly, anatomising foliation characterises the clay matrix (Fig. 7), with folds and shear planes similar in appearance to previously described S–C fabric in these rocks (Fig. 8 in Bradbury et al., 2011), and shear bands developed in ductile, experimentally deformed clay-rich material (Fig. 7; Dehandschutter et al., 2004). Alternatively, these shears could also present remnants of older P and R shear sets that were reactivated during ductile flow of the clay matrix.

### 3.4. TEM observations

TEM fringe imaging of the clay coated shear fractures (seen in Fig. 3b) prepared as FIB lamella reveals abundant deformation microstructures within the smectite packets (Fig. 8). Although the resolution is not great enough to resolve individual tetrahedral and octahedral sheets, the location of interlayers and particle surfaces can be recognized based on contrast features. Lattice-parallel slip along these planes offsets lattice areas with minor strain (Fig. 8), and is commonly associated with layer terminations that are inferred to form by migration of edge dislocations in areas of the strained crystal lattice (Bell, 1986). Such microstructures are described in smectitic clay gouges and deformed phyllosilicate rocks in a variety of fault zones (Warr and Cox, 2001; Solum et al., 2003; Schleicher et al., 2012; Viti et al., 2014).

Although the small clay–mineral particle size offers more potential for slip along hydrated particles surfaces, an important property of smectite is that every single lattice layer, if hydrated, can be a potential slip surface. TEM observations of the spacing of parallel slip surfaces show planes 3–5 lattice layers (<8 nm) apart

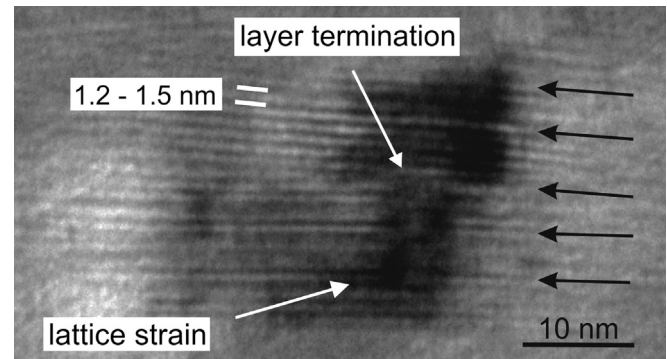


Fig. 8. Transmission-electron image of deformed Mg-smectite particles lying along clay-coated shear fractures. Black arrows mark the position of slip planes along interlayer surfaces recognized by lattice strain offsets.

in the 00 $l$  direction (Fig. 8a), indicating shear was accommodated via pervasive slip. SAED patterns confirm the turbostatic nature of the smectite patterns, with only diffuse ordering in the 00 $l$  direction.

## 4. Discussion

### 4.1. Analytical approach

In this first FIB–SEM study of SAFOD Central Deforming Zone clay gouge, we detail the microstructures and microchemical variations that occur between clasts, clay-coated slip surfaces and matrix clay. Due to the high degree of analytical difficulty in studying smectite-rich materials, which are particularly susceptible to rapid electron beam damage, and due to the large investment of time and expense involved in applying the “slice-and-view” technique, we have purposely focused on characterizing the heterogeneities of a specific sample of scientific interest. This strategy is more valuable than spreading the same number of observations over multiple sample sets that would lack the current tight sample constraints. Still, we acknowledge the importance of extending our detailed work to a larger sample suite. The interpretations made in this study therefore apply strictly to the processes relevant to the G4, section 4, core of the Central Deforming Zone. However, given

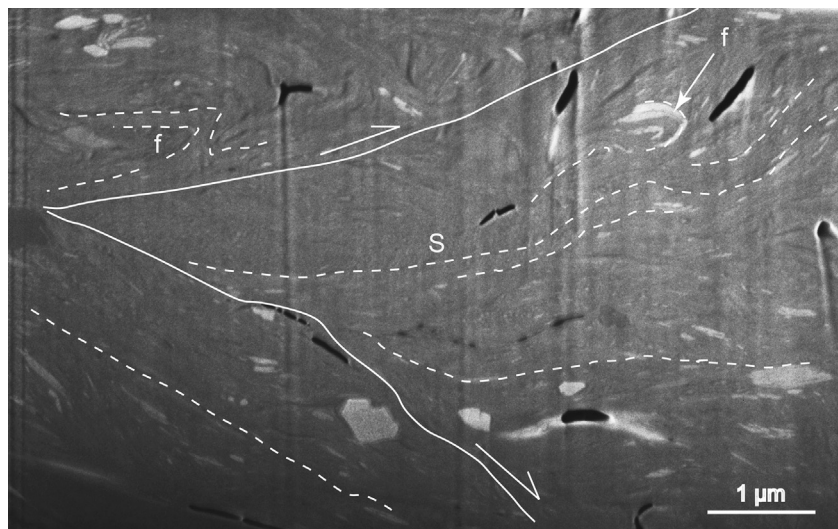
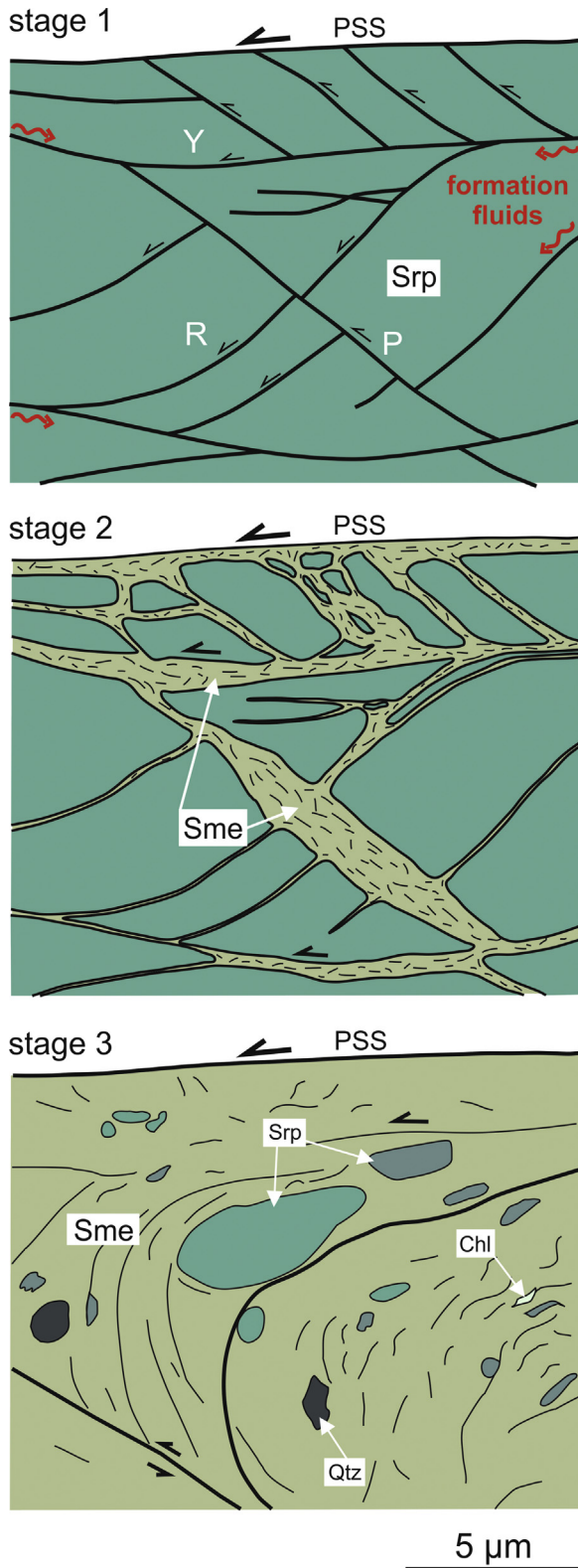


Fig. 7. In-lens BSE electron image of the smectite-rich matrix of the G44 sample. The low contrast grey of the smectite comprises over 80% of the gouge matrix and shows a characteristic anatomising fabric (S) cut by shear planes (solid lines). The shear planes intersect at angles <30°. Tight folds in the clay fabric are also evident (f). The vertical lines are artefacts of the milling process.



**Fig. 9.** Model for the three-stage development of fault weakening of the San Andreas Fault at Parkfield. Stage 1: generation of brittle shear fractures, microseismicity and infiltration of formation fluids. Stage 2: Fracture-controlled growth of smectite on shear planes and the onset of creep motion. PSS = principal slip surface, P = pressure (thrust) shear, R = Riedel shear, Y = shear parallel to principle slip surface. Stage 3: Development of abundant (>80%) smectite matrix with slip accommodated by ductile flow along the clay fabric with local shear bands and folding. Srp = serpentine, Sme = Smectite, Qtz = quartz, Chl = chlorite.

the particularly weak mechanical behaviour of this material in the laboratory, we consider it also appropriate to use our findings to develop a hypothesis for the controls of creep in the fault zone as a whole. Furthermore, our sample comes from the well mapped Central Deforming Zone gouge zone that generally exhibits similar behaviour (Carpenter et al., 2012).

A number of features described in this clay gouge are previously recognised in SAFOD core material at a variety of scales both inside and adjacent to the creep zones (Bradbury et al., 2011; Holdsworth et al., 2011). They include the tight networks of anastomosing clay fabric (Bradbury et al., 2011; Holdsworth et al., 2011; Janssen et al., 2012), with sets of R and P shears (Hadizadeh et al., 2012) or S–C fabrics (Bradbury et al., 2011), the abundance of clay-coated polished slip surfaces with slickenfibres (Schleicher et al., 2010) and lens-shaped clasts oriented parallel to the clay fabric (Sill, 2010). However, with the improved control of the FIB–SEM method, the development of clay-fabric and fault lubrication by smectite down to the nanometre-scale of observation may be reconstructed because the components of the gouge: namely the clasts, the slip surfaces and the intervening clay matrix, can be characterized at this finer scale. Based on our 3D microscopic characterization of the G44 sample, it is evident that the very low material strength results from a combination of smectite clay growth and clay fabric development.

A particularly important location for showing the transition from brittle-deforming serpentine to ductile deforming clay is the external, clay-coated fracture surfaces of cm-sized, flattened serpentine clasts (Figs. 3b, 4c and 6). Here, strong strain partitioning between clast and matrix resulted in fracturing and fracture-controlled, substrate clay growth reflecting the generation of clay fabric during fluid-controlled alteration of the clast material.

#### 4.2. Model of clay fabric evolution

Our observations are used to reconstruct a three-stage model of clay fabric evolution for this weak gouge (Fig. 9), which is proposed as an important underlying mechanism of weakening along the central section of the San Andreas Fault. The initial stage (1) of fault-gouge deformation involves seismogenic fracturing of serpentine bodies and associated shale lithologies that generates fresh shear fracture networks as a prerequisite to the formation of clay gouge (Fig. 9). The intact serpentine appears to be only weakly deformed and mechanically rigid due to the intact shape of serpentine grains, despite notable amounts of alteration to Mg-smectite (Figs. 4a and 5). This alteration (up to 22% by area) occurs scattered around the serpentine and as disseminated alteration within the grains that results in a close to random clay fabric. The lack of a good interconnect clay fabric within the clasts is considered to be the reason why these grains are significantly less deformed than the surrounding clay matrix in the same way that deformed random powders are mechanically stronger than equivalent intact wafers with good phyllosilicate (clay) fabric (Collettini et al., 2009; Ikari et al., 2011a).

In contrast, the flattened, polished sheared margins of clasts show a well-developed set of shear fractures including R, P and Y shears. The formation of Riedel shears in laboratory-deformed serpentine is a feature considered to occur during seismogenic slip as opposed to the more distributed nature of aseismic deformation fabrics (Reinen, 2000). The observations are in accordance with documented evidence of past seismicity in the rocks surrounding the Central Deforming Zone (Bradbury et al., 2011). Such repeated fracturing could occur during periodic M6+ type earthquakes, whereby subsequent fracture reactivations may be generating the repeating micro-seismicity (<M3), consistent with micro-earthquakes recorded along the Southwest Deforming Zone and Northern Bounding Fault (Fig. 1b).

The generation of R, P and Y shears at the sub-micrometre scales is an important requirement for allowing fluids, probably derived from local formation waters, to penetratively infiltrate the low permeability fault-gouge that drives subsequent dissolution and precipitation reactions in a metasomatic exchange process (Lockner et al., 2011; Moore and Rymer, 2012; Moore and Lockner, 2013). The alteration of serpentine to Mg-smectite (saponite) is a process favoured by alkaline hydrous fluids (Moore and Lockner, 2013), whereby high pH conditions (>10), characteristic of groundwaters associated with ultramafic bodies, are required for the dissolution and transport of Al and Si required for smectite growth. The supply of Al is critical in the formation of saponite that replaces Mg in the octahedral sites and generates the tetrahedral charge deficient characteristic of this trioctahedral smectite and the 3D structural ordering of water molecules (Suquet et al., 1975) responsible for the notably weak behaviour of this hydrated smectite phase.

In the second stage (2) of development, localized clay nano-coatings on shear fractures surfaces lead to the onset of creep motion with growth of both platy and fibrous smectite aligned in the direction of slip (Fig. 9). This alignment is alone unlikely to result from particle rotation and indicates substrate-controlled growth of smectite that is synchronous with motion along these surfaces (Fig. 3b). The occurrence of these coatings of smectitic minerals on fracture surfaces supports the clay nanocoatings model of Schleicher et al. (2010). The characteristic polished and striated fracture surfaces are not considered to result from dewatering and volume loss as suggested by Holdsworth et al. (2011) where samples lack striated surfaces, but are clearly original deformation microstructures characteristic of SAFOD fault gouge. Such fine fabric elements in the gouge have not been detected by bulk textural methods that measure the combined signals of both fracture-related and pore-filling matrix clay minerals (Janssen et al., 2012).

In the case of the shear fracture network developed at the sheared clast margins, the principal planes of displacement and their parallel Y-shears are likely to accommodate the main displacements, whereby the R and P shears are less active as they cannot accommodate significant displacements without further fracturing of the clast material: a process that would lead to strain hardening. That slip is focused along sets of sub-parallel shears is supported by the abundance of fault striations and slickenfibres on these planes (Fig. 3a–b). Also, TEM imaging of the oriented smectite particles along these planes indicates that pervasive slip occurs at the lattice scale along interlayers and associated particle surfaces (Fig. 8). Hydrated smectites are expected to show similar lubrication behaviour as described for sheared graphite, whereby the effective area of an embedded weak phase is significantly increased by smearing along a narrow planar slip zone or an interconnected network (Rutter et al., 2013). Extensive smearing along these surfaces within the clay-gouge is therefore suggested as the primary mechanism of creep in the fault zone as long as sufficient interconnected clay-coated foliation is developed (Schleicher et al., 2010). Based on these relationships, it may be predicted that fault segments currently producing micro-earthquakes could evolve into aseismically creeping fault segments once clay fabrics become adequately developed. We conclude that seismogenic shear fracturing with the generation of R, P and Y shears, fluid-infiltration and subsequent deformation-controlled clay fabric development are key requirements that promote aseismic creep, which are mechanisms that operate in addition to pressure solution deformation (Holdsworth et al., 2011; Gratier et al., 2011). A similar mechanism of fracturing, clay neoformation, and clay fabric development have been proposed for other types of fault-rock settings, such as in Alpine reverse faulting of Opalinus Clay in the Jura Mountains of Switzerland (Laurich et al., 2014).

A third stage (3) of fabric evolution is recognizable by continuing dissolution–precipitation alteration of serpentine, chlorite, quartz and calcite clasts, which results in a massive smectitic matrix (>80%; Figs. 4c, 7 and 9). Deformation of the matrix clay is more likely to be strongly controlled by mechanical rotation of clay particles rather than by substrate-controlled growth mechanism, with the development of anastomosing slip surfaces, resulting in a scaly, anastomosing fabric defined by sets of shears planes that intersect at low angles (Fig. 7). Creep is presumably maintained by ductile flow of the matrix with minimal fracturing of the remaining clast material. Ductile deformation also results in localized folding of the matrix and rotation of elongated clasts to lie parallel with the foliation. The smooth and rounded edges of the clast material probably reflect intense dissolution at the grain boundaries and expansive alteration to smectite (Fig. 4c).

Another feature considered favourable for clay-controlled creep is the type of cation present in the hydrated interlayer sites of smectite. In Mg-smectite (such as saponite), the Mg cations derived from dissolution of the serpentine together with Ca cations derived from adjacent shale lithologies are primary cations occupying the hydrated interlayer sites. Hydration phase diagrams and molecular simulations by Monte Carlo modelling of smectite indicate the predicted structure of hydrated Ca-bearing water layers at 2.7 km crustal depth should be the 1 water-layer structure with a lattice thickness of 1.18 nm (De Pablo et al., 2007). Based on the location of slip planes observed at the crystal scale, it is confirmed that slip occurs primarily along the Mg- and Ca-occupied hydrated interlayers whereby displacements are spaced at 3–5 lattice layers apart (Fig. 8). As current molecular models indicate that divalent ions concentrate around a medium line, with the water molecules protruding outwards toward the negatively charged interlayer surfaces, slip can be easily accommodated by the breakage and rebuilding of weak hydrogen bonds. In fact, only hydration of divalent interlayer cations have so far yielded friction coefficients equivalent to those measured for the creeping gouge, whereby the type of interlayer cation and its hydration structure explain the weak behaviour of smectite in laboratory shear experiments (Behnsen and Faulkner, 2013; Ikari et al., 2007). We posit that in addition to clay fabric, the state of cation hydration is a key contributor to creep along the SAFOD segment at ~2.7 km depth and the origin of fault weakness as measured under laboratory conditions.

Whereas it is evident that the formation of smectite fabric plays a prime role in the weakness of fault creep gouge samples at ~2.7 km vertical depth, much speculation exists concerning phase transitions occur at greater crustal depths. Based on the occurrence of talc in some exhumed fault sections of ultramafic rocks along the San Andreas Fault, this weak Mg-phylosilicate has been used to explain creep at depths below the cored section (Moore and Rymer, 2012). In contrast, smectitic phases are argued to persist to significantly deep crustal depths (10–12 km) in the form of weak chlorite–smectite phases that are similarly produced by reactions between ultramafic and clastic sedimentary rocks (Schleicher et al., 2012). Whatever the types of phyllosilicate mineral assemblages present at greater depth, we conclude that similar mechanisms of fault-rock fabric generation and smearing of weak phases along interconnected principle slip surfaces and Y-shears are likely to remain the important mechanism at depths beneath that cored in the SAFOD project.

## 5. Conclusions

1. 3D nano-analytical reconstructions of the distribution of clay minerals developed in some of the weakest SAFOD fault gouge, sampled from the G4, section 4, core of the creeping section of

the Central Deforming Zone at ~3298 m measured borehole depth, reveal a variety of shear fabrics that directly reflect changes in strength and seismic behaviour.

- We posit that fault creep initiated in our samples by formation of interconnected nano-coatings formed by fracture-controlled, substrate growth of Mg-smectite on R, P and Y shear surfaces, whereby slip could be accommodated by lubrication along parallel sets of shears without extensive fracturing of clasts. The notably weak behaviour of this smectite can be attributed to the predominance of hydrated Mg- and Ca-interlayer cations and the 3D structural ordering of water molecules caused by the tetrahedral charge deficiency of this trioctahedral smectite (saponite) formed by the octahedral substitution of Mg by Al. At the atomic scale, pervasive slip occurs along closely-spaced hydrated smectite surfaces with displacements spaced at 3–5 lattice layers apart.
- Serpentine clasts, although also altered to Mg-smectite, are only weakly deformed but show signs of intense dissolution at grain boundaries. Microscopic-scale grain rotations of the clasts locally contribute to the clay matrix fabric.
- The strength and seismic behaviour of the central section of the San Andreas Fault in California is proposed to evolve as clay fabrics develop with accumulated fault slip. A three-stage model of clay fabric evolution is proposed for the G44 creep gouge that highlights how this strand of the fault is controlled by the development of interconnected clay fabric that now lubricates fault motion.

#### Author contribution

LNW obtained and interpreted the FIB–SEM results and is principle author of the paper. JW is responsible for 3D analysis of the “slice-and-view” data and BMC for conducting the rock deformation experiments. All authors contributed to the writing of the paper.

#### Acknowledgements

We thank Cecilia Viti and Peter Vrolijk for their constructive reviews. LNW acknowledges the financial support for the purchase of a Zeiss Auriga FIB–SEM microscope (Großgeräte der Länder: GZ: INST 292/102-1 LAGG), BvdP and AMS acknowledge NSF support (most recently, EAR 1118704) for their continuing work on clay mineralogy and fabrics in fault rocks. CJM and BMC acknowledge NSF support under awards EAR-0950517, EAR1045825, and EAR1215856.

#### References

- Behnen, J., Faulkner, D.R., 2013. Permeability and frictional strength of cation-exchanged montmorillonite. *J. Geophys. Res. Solid Earth* 118, 2788.
- Bell, T.E., 1986. Microstructure in mixed-layered illite/smectite and its relationship to the reaction of smectite to illite. *Clays Clay Miner.* 34, 146–154.
- Bos, B., Spiers, C.J., 2001. Experimental investigation into the microstructural and mechanical evolution of phyllosilicate-bearing fault rock under conditions favouring pressure solution. *J. Struct. Geol.* 23, 1187–1202.
- Bradbury, K.K., Evans, J.P., Chester, J.S., Chester, F.M., Kirshner, D.L., 2011. Lithology and internal structure of the San Andreas Fault at depth based on characterization of phase 3 whole-rock core in the San Andreas Fault Observatory at Depth (SAFOD) borehole. *Earth Planet. Sci. Lett.* 310, 131–144.
- Carpenter, B.M., Marone, C., Saffer, D.M., 2009. Frictional behavior of materials in the 3D SAFOD volume. *Geophys. Res. Lett.* 36, L05302.
- Carpenter, B.M., Marone, C., Saffer, D.M., 2011. Frictional strength of the San Andreas fault from laboratory measurements of SAFOD drill samples. *Nat. Geosci.* 4, 251–254.
- Carpenter, B.M., Saffer, D.M., Marone, C., 2012. Frictional properties and sliding stability of the San Andreas fault from deep drill core. *Geology* 40, 759–762.
- Collettini, C., Niemeijer, A., Viti, C., Marone, C., 2009. Fault zone fabric and fault weakness. *Nature* 406, 907–910.
- De Pablo, L., Chavez, M.L., Monsalvo, R., 2007. The state of hydration of Ca-exchanged montmorillonite at a depth of 2–2.7 kilometers. *Can. Mineral.* 45, 481–492.
- Dehandschutter, B., Vandycke, S., Sintubin, M., Vandenberghe, N., Wouters, L., 2004. Brittle fractures and ductile shear bands in argillaceous sediments: inferences from Oligocene Boom Clay (Belgium). *J. Struct. Geol.* 27 (6), 1095–1112.
- Egerton, R.F., Li, M., Malac, P., 2004. Radiation damage in the TEM and SEM. *Micron* 35, 399–409.
- Gratier, J.-P., Richard, J., Renard, F., Mittempergher, S., Doan, M.-L., Di Toro, G., Hadizadeh, J., Boullier, A.-M., 2011. Aseismic sliding of active faults by pressure solution creep: evidence from the San Andreas Fault Observatory at Depth. *Geology* 39, 1131–1134.
- Hadizadeh, J., Mittempergher, S., Gratier, J.-P., Renard, F., Di Toro, G., Richard, J., Babaie, H.A., 2012. A microstructural study of fault rocks from the SAFOD: implications for the deformation mechanisms and strength of the creeping segment of the San Andreas Fault. *J. Struct. Geol.* 42, 246–260.
- Haines, S., Kaproth, B., Marone, C., Saffer, D., van der Pluijm, B., 2013. Shear zones in clay-rich fault gouge: a laboratory study of fabric development and evolution. *J. Struct. Geol.* 51, 205–225.
- Hickman, S., Zoback, M., Ellsworth, W., Boness, N., Malin, P., 2007. Structure and Properties of the San Andreas Fault in Central California: Recent Results from the SAFOD Experiment. USGS staff – Published Research Paper 421, pp. 29–32.
- Holdsworth, R.E., 2004. Weak faults – rotten cores. *Science* 30, 181–182.
- Holdsworth, R.E., van Diggelen, E.W.E., Spiers, C.J., de Bresser, J.H.P., Walker, R.J., Bowen, L., 2011. Fault rocks from the SAFOD core samples: implications for weakening at shallow depths along the San Andreas fault, California. *J. Struct. Geol.* 33, 132–144.
- Ikari, M.J., Saffer, D.M., Marone, C., 2007. Effect of hydration state on the frictional properties of montmorillonite-based fault gouge. *J. Geophys. Res.* 112, B06423.
- Ikari, M.J., Niemeijer, A., Marone, C., 2011a. The role of fault zone fabric and lithification state on frictional strength, constitutive behavior, and deformation microstructure. *J. Geophys. Res.* 116 <http://dx.doi.org/10.1029/2011JB008264>.
- Ikari, M.J., Marone, C., Saffer, D.M., 2011b. On the relation between fault strength and frictional stability. *Geology* 39, 83–86. <http://dx.doi.org/10.1130/G31416>.
- Janssen, C., Wirth, R., Reinicke, A., Rybacki, E., Naumann, R., 2010. Nanoscale porosity in SAFOD core samples (San Andreas Fault). *Earth Planet. Sci. Lett.* 301 (1–2), 179–189.
- Janssen, C., Kanitpanyacharoen, W., Wenk, H.-R., Wirth, R., Morales, L., Rybacki, E., Kienast, M., Dresen, G., Reinicke, A., 2012. Clay fabrics in SAFOD core samples. *J. Struct. Geol.* 43, 118–127.
- Janssen, C., Wirth, R., Wenk, H.-R., Morales, L., Naumann, R., Kienast, M., Song, S., Dresen, G., 2014. Faulting processes in active faults – evidence from TCDP and SAFOD drill core samples. *J. Struct. Geol.* 65, 100–116.
- Laurich, B., Urai, J.L., Besbois, G., Vollmer, C., Nussbaum, C., 2014. Microstructural evolution of an incipient fault zone in Opalinus Clay: insights from an optical and electron microscopic study of ion-beam polished samples from the Main Fault in the Mt-Terri Underground Research Laboratory. *J. Struct. Geol.* 67, 107–128.
- Lockner, D.A., Morrow, C., Moore, D., Hickman, S., 2011. Low strength of deep San Andreas fault gouge from SAFOD core. *Nature* 472, 82–85.
- Marone, C., Richardson, E., 2010. Learning to read fault-slip behavior from fault-zone structure. *Geology* 38, 767–768.
- Mayer, J., Giannuzzi, L.A., Kamino, T., Michael, J., 2007. TEM preparation and FIB-induced damage. *MRS Bull.* 32, 400–407.
- Moore, D.E., Lockner, D.A., 2013. Chemical controls on fault behavior: weakening of serpentinite sheared against quartz-bearing rocks and its significance for fault creep in the San Andreas system. *J. Geophys. Res. Solid Earth* 118, 1–13.
- Moore, D.M., Reynolds, R.C., 1997. X-ray Diffraction and the Identification of Clay Minerals. Oxford University Press, p. 378.
- Moore, D.E., Rymer, M.J., 2007. Talc-bearing serpentinite and the creeping section of the San Andreas fault. *Lett. Nat.* 448, 795–797.
- Moore, D.E., Rymer, M.J., 2012. Correlation of clayey gouge in a surface exposure of serpentinite in the San Andreas Fault with gouge from the San Andreas Fault Observatory at Depth (SAFOD). *J. Struct. Geol.* 38, 51–60.
- Morrow, C.A., Lockner, A., Hickman, S., 2013. Deep permeability of the San Andreas fault from San Andreas fault observatory at depth (SAFOD) core samples. *J. Struct. Geol.* <http://dx.doi.org/10.1016/j.jsg.2013.09.009>.
- Nadeau, R.M., Michelini, A., Uhrhammer, R.A., Dolenc, D., McEvilly, T.V., 2004. Detailed kinematics, structure, and recurrence of microseismicity in the SAFOD target region. *Geophys. Res. Lett.* 31, L12S08.
- Niemeijer, A.R., Spiers, C.J., 2006. Velocity, dependence of strength and healing behaviour in simulated phyllosilicate-bearing fault gouge. *Tectonophysics* 427, 231–253.
- Niemeijer, A.R., Marone, C., Elsworth, D., 2010. Fabric induced weakness of tectonic faults. *Geophys. Res. Lett.* 37, L03304. <http://dx.doi.org/10.1029/2009GL041689>.
- Reinen, L.A., 2000. Seismic and aseismic slip indicators in serpentine gouge. *Geology* 28, 135–138.
- Rutter, E.H., Hackston, A.J., Yeatman, E., Brodie, K.H., Mecklenburgh, J., May, S.E., 2013. Reduction of friction on geological faults by weak-phase smearing. *J. Struct. Geol.* 51, 52–60.
- Schleicher, A.M., van der Pluijm, B.A., Warr, L.N., 2006. Origin and significance of clay-coated fractures in mudrock fragments of the SAFOD borehole (Parkfield, California). *Geophys. Res. Lett.* 33, L16313–L16317.
- Schleicher, A.M., van der Pluijm, B.A., Warr, L.N., 2010. Nano-coatings of clay and creep of the San Andreas Fault at Parkfield, California. *Geology* 38, 667–670.

- Schleicher, A.M., van der Pluijm, B.A., Warr, L.N., 2012. Chlorite–smectite clay minerals and fault behavior: new evidence from the San Andreas Fault Observatory at Depth (SAFOD) core. *Lithosphere* 4, 209–220.
- Scholz, C.H., 2002. *The Mechanics of Earthquakes and Faulting*. Cambridge University Press, ISBN 0521655404, p. 471.
- Sill, D.W., 2010. The Fabric of Clasts, Veins and Foliations within the Actively Creeping Zones of the San Andreas Fault at SAFOD: Implications for Deformation Processes. A&M University, College Station, TX, p. 81.
- Solum, J.G., van der Pluijm, B.A., Peacor, D.R., Warr, L.N., 2003. Influence of phyllosilicate mineral assemblages, fabrics, and fluids on the behavior of the Punchbowl fault, southern California. *J. Geophys. Res.* 108 (B5), 2233.
- Solum, J., Hickman, S., Lockner, D.A., Moore, D.E., van der Pluijm, B.A., Schleicher, A.M., Evans, J.P., 2006. Mineralogical characterization of protolith and fault rocks from the SAFOD main hole. *J. Geophys. Res. Lett.* 33, L21314.
- Suquet, H., De La Calle, C., Pezerat, H., 1975. Swelling and structural organization of saponite. *Clays Clay Miner.* 23, 1–9.
- Titus, S.J., DeMets, C., Tikoff, B., 2006. Thirty-five-year creep rates for the creeping segment of the San Andreas fault and the effects of the 2004 Parkfield earthquake: constraints from alignment arrays, continuous global positioning system, and creep meters. *Bull. Seismol. Soc. Am.* 96 (4B), S250–S268.
- Viti, C., Collettini, C., Tesei, T., 2014. Pressure solution seams in carbonatic fault rocks: mineralogy, micro/nanostructures and deformation mechanisms. *Contrib. Mineral. Petrol.* 167, 970.
- Warr, L.N., Cox, S., 2001. Clay mineral transformations and weakening mechanisms along the Alpine Fault, New Zealand. In: Holdsworth, R.E., Strachan, R.A., Magloughlin, J., Knipe, R.J. (Eds.), *The Nature and Tectonic Significance of Fault Zone Weakening*. Geological Society London Special Publication, vol. 186, pp. 85–101.
- Warr, L.N., Grathoff, G., 2011. Geoscientific applications of particle detection and imaging techniques with special focus on the monitoring clay mineral reactions. In: Grupen, C. (Ed.), *Handbook of Particle Detection*. Springer, ISBN 978-3-642-13270-4.
- Wibberley, C., 2007. Talc at fault. *Nature* 448, 756–757.
- Wirth, R., 2009. Focused ion beam (FIB) combined with SEM and TEM: advanced analytical tools for studies of chemical composition, microstructure and crystal structure in geomaterials on a nanometer scale. *Chem. Geol.* 261 (3–4), 217–229.
- Zoback, M.D., Zoback, M.L., Mount, Van S., Suppe, J., Eaton, J.P., Healy, J.H., Oppenheimer, D., Reasenber, P., Jones, L., Raleigh, C.B., Wong, I., Scotti, O., Wentworth, C., 1987. New evidence on the state of stress of the San Andreas fault system. *Science* 238, 1105–1111.
- Zoback, M., Hickman, S., Ellsworth, W., 2011. Scientific drilling into the San Andreas Fault Zone – an overview of SAFOD's first five years. *Sci. Drill.* 11, 14–28.